Determination of the astrophysical S factor for $^{11}C(p,\gamma)^{12}N$ from the $^{12}N \rightarrow {}^{11}C+p$ asymptotic normalization coefficient

Xiaodong Tang,* A. Azhari, C. A. Gagliardi, A. M. Mukhamedzhanov, F. Pirlepesov, L. Trache, and R. E. Tribble
Cyclotron Institute, Texas A&M University, College Station, Texas 77843

V. Burjan and V. Kroha
Institute of Nuclear Physics, Czech Academy of Sciences, Prague-Řež, Czech Republic

F. Carstoiu
Institute of Physics and Nuclear Engineering H. Hulubei, Bucharest, Romania

(Received 20 September 2002; published 22 January 2003)

The evolution of very low-metallicity, massive stars depends critically on the amount of CNO nuclei that they produce. Alternative paths from the slow 3α process to produce CNO seed nuclei could change their fate. The $^{11}C(p,\gamma)^{12}N$ reaction is an important branch point in one such alternative path. At energies appropriate to stellar evolution of very low-metallicity, massive stars, nonresonant capture dominates the reaction rate. We have determined the astrophysical S factor for the $^{11}C(p,\gamma)^{12}N$ reaction using the asymptotic normalization coefficient for $^{12}N \rightarrow {}^{11}C+p$ to fix the nonresonant capture rate. In our experiment, a 110 MeV ^{11}C radioactive beam was used to study the $^{14}N(^{11}C,{}^{12}N)^{13}C$ peripheral transfer reaction and the asymptotic normalization coefficient, $(C^{^{12}N}_{p_{eff}})^2=(C^{^{12}N}_{p_{1/2}})^2+(C^{^{12}N}_{p_{3/2}})^2=1.73\pm0.25$ fm^{-1}, was extracted from the measured cross section. The contributions from the second resonance and interference effects were estimated using an R-matrix approach with the measured asymptotic normalization coefficient and the latest value for Γ_γ. We find the S factor for $^{11}C(p,\gamma)^{12}N$ is significantly larger than previous estimates. As a result, the required density for it to contribute is reduced, and more CNO material may be produced.

DOI: 10.1103/PhysRevC.67.015804 PACS number(s): 26.30.+k, 25.60.Je, 25.40.Lw, 25.60.Bx

I. INTRODUCTION

It has been known for many years that very massive stars may have formed in the early Universe when the only seed material available consisted of hydrogen and helium nuclei. In 1986, Fuller, Woosley, and Weaver [1] studied the evolution of radiation-dominated super-massive stars with a hydrodynamic code KEPLER, in which they considered the traditional pp chains, the triple-alpha process, the CNO cycle and the rp process. Early on the stars were in a quasistatic stage with a balance between thermal expansion and gravitational contraction. After the stars ran out of pp chain fuel, they began to contract. Typically, the triple-alpha process turned on too late to prevent the supermassive stars from collapsing to black holes without exploding, but Fuller *et al.* found that a significant primordial abundance of CNO nuclei could slow the contraction long enough to permit the stars to explode.

In 1989 Wiescher, Buchmann, and Thielemann [2] reinvestigated the reaction rates for nuclei up to oxygen. They suggested several reaction sequences that would permit very massive stars to bypass the 3α process. They determined the required temperature and density conditions where capture reactions on short lived nuclei were of equal strength to competing β decays or inverse photo-disintegration. They found that the $^3He(\alpha,\gamma)^7Be(\alpha,\gamma)^{11}C$ reactions could represent an important path from helium to carbon isotopes. The ^{11}C produced in this sequence may decay and return to ^4He via $^{11}C(\beta^+\nu)^{11}B(p,\alpha)^8Be(^4He,^4He)$ or be depleted by proton capture into the $A \geqslant 12$ region through $^{11}C\ (p,\gamma)^{12}N$.

An open question in the early evolution of the universe is whether very massive primordial stars contributed any significant material to later generations of stars. Recent calculations using standard reaction sequences indicate that nonrotating stars with masses greater than 260 solar masses and zero metallicity undergo gravitational collapse to black holes without losing any mass [3]. However, the results are very sensitive to the initial CNO mass fraction. Fractions as small as 10^{-8} greatly change the nuclear energy generation rate. Therefore, processing even a small fraction of the relic deuterium and ^3He from the Big Bang into CNO material might have an impact on the stellar evolution if it occurs sufficiently early in the life of the massive star. In order to determine if the hot pp chain reactions play any significant role in the evolution of massive stars by providing a means to produce CNO nuclei prior to helium burning, it is important to determine the rates of the key reactions.

In the $^{11}C\ (p,\gamma)^{12}N$ reaction, direct capture into the ground state of ^{12}N and resonant capture into the first and second excited states dominate the reaction rate at stellar energies (see Fig. 1). Several indirect methods have been used to determine the parameters for this capture reaction. Based on the lifetime of the first excited state of ^{12}B, Wiescher *et al.* derived a value $\Gamma_\gamma=2.6$ meV for the radiative width of the first excited state in ^{12}N. Since no experimental γ transition data were available for the higher excited states, they used the Weisskopf limit as an estimate for the radiative width of the second excited state. In both cases, a 100% branching ratio to the ground state of ^{12}N was assumed.

*Electronic address: tangxd@comp.tamu.edu

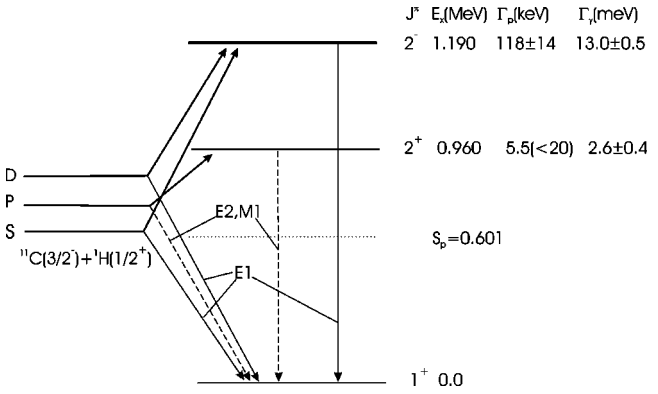

FIG. 1. Low lying energy levels of ^{12}N and the radiative capture process ^{11}C$(p,\gamma)^{12}$N. The solid lines leading to the ground state are $E1$ transitions. The dashed lines leading to the ground state are $E2$ and $M1$ transitions. The resonance parameters used in this paper are shown on the right side of the figure.

According to their calculation, the ^{11}C $(p,\gamma)^{12}$N reaction will occur when $0.2<T_9<0.4$, where T_9 is the temperature in units of 10^9 K, and the second resonance does not contribute significantly to the reaction rate within this temperature region.

Subsequently, a group at GANIL [4] used Coulomb breakup of ^{12}N on ^{208}Pb to measure the parameters needed to determine the capture reaction rate. By fitting the relative energy spectrum of ^{11}C$+p$, they derived Γ_γ for the 2^- second excited state ($6.0^{+7}_{-3.5}$ meV), and obtained a spectroscopic factor (0.40 ± 0.25) that they used to calculate the direct capture rate. The 2^+ first excited state in ^{12}N decays through an $M1+E2$ transition. The $M1$ decay mode is expected to dominate based on the behavior of the analog level in the mirror nucleus ^{12}B. However, the $E2$ Coulomb excitation is about 1000 times larger than the $M1$ excitation, so a small $E2$ admixture would give a larger Coulomb breakup contribution than that due to the $M1$ transition. Since the value of the mixing ratio is not precisely known, it is impossible to extract a radiative width for the 2^+ state from their experiment. With their experimental data, they concluded that the main contribution to the S factor in the region below $T_9=0.3$ comes from direct capture and above this temperature resonance population of the first excited state begins to dominate.

There are two shortcomings of the GANIL result. One is the 60% uncertainty of the spectroscopic factor. The other is that they neglected the interference between direct capture and resonant capture to the broad second excited state. This interference could make up to a 20% contribution to the reaction rate according to their data. Also, a recent preliminary result for ^{12}N Coulomb dissociation carried out at RIKEN [5] showed that the γ width of the 2^- state is 13 ± 0.5 meV, a factor of two larger than the GANIL central value.

We have used the peripheral transfer reaction, ^{14}N(^{11}C, ^{12}N)^{13}C at 10 MeV/nucleon, to measure the asymptotic normalization constant (ANC) for ^{12}N$\rightarrow^{11}$C $+p$, and then determined the capture rate for ^{11}C $(p,\gamma)^{12}$N from the measured ANC and the latest parameters available for the resonance states in an R-matrix analysis.

II. *R*-MATRIX ANALYSIS FOR ^{11}C $(p,\gamma)^{12}$N

Let us consider the radiative capture reaction $B+b\rightarrow A+\gamma$. The R-matrix radiative capture cross section to a state of nucleus A with a given spin J_f is given by [6]

$$\sigma_{J_f}=\frac{\pi}{k^2}\sum_{J_iIl_i}\frac{2J_i+1}{(2J_b+1)(2J_B+1)}\,|U_{Il_iJ_fJ_i}|^2. \qquad (1)$$

J_i is the total angular momentum of the colliding nuclei in the initial state, J_b and J_B are their spins, and I, k, and l_i are their channel spin, relative momentum and orbital angular momentum.

$U_{Il_iJ_fJ_i}$ is the transition amplitude from the initial continuum state to the final bound state. It is given by the sum of the resonant and nonresonant transition amplitudes. The amplitudes only interfere if they have the same channel spin I and orbital angular momentum l_i. In the one-level, one-channel approximation, the resonant amplitude for the capture into the resonance with energy E_R and spin J_i, and subsequent decay into the bound state with spin J_f, is given by

$$U^R_{Il_iJ_fJ_i}=-ie^{i(\omega_{l_i}-\phi_{l_i})}\,\frac{[\Gamma^{J_i}_{bIl_i}(E)]^{1/2}\,[\Gamma^{J_i}_{\gamma J_f}(E)]^{1/2}}{E-E_R+i\,\dfrac{\Gamma_{J_i}}{2}}. \qquad (2)$$

Here E is the relative energy, ϕ_{l_i} is the solid sphere scattering phase shift in the l_i-th partial wave. The phase factor ω_{l_i} is given by

$$\omega_{l_i}=\sum_{n=1}^{l_i}\tan^{-1}\left(\frac{\eta_i}{n}\right), \qquad (3)$$

$[\Gamma^{J_i}_{bIl_i}(E)]^{1/2}$ is real and its square is the observable partial width of the resonance in the channel $B+b$ with the given set of quantum numbers, $[\Gamma^{J_i}_{\gamma J_f}(E)]^{1/2}$ is complex and its modulus square is the observable radiative width. $\eta_i=Z_b\,Z_B\,\mu_{Bb}/k$ is the Coulomb parameter in the initial state, and μ_{Bb} is the reduced mass of particles B and b. The energy dependence of the partial and radiative widths are given by

$$\Gamma^{J_i}_{bIl_i}(E)=\frac{P_{l_i}(E)}{P_{l_i}(E_R)}\,\Gamma^{J_i}_{bIl_i}(E_R) \qquad (4)$$

and

$$\Gamma^{J_i}_{\gamma\,J_f}(E)=\left(\frac{E+\varepsilon_f}{E_R+\varepsilon_f}\right)^{2L+1}\Gamma^{J_i}_{\gamma\,J_f}(E_R), \qquad (5)$$

respectively. $\Gamma^{J_i}_{bIl_i}(E_R)$ and $\Gamma^{J_i}_{\gamma\,J_f}(E_R)$ are the experimental partial and radiative resonance widths, P_l is the penetrability, ε_f is the proton binding energy of the bound state in nucleus A, and L is the multipolarity of the gamma transition.

The nonresonant capture amplitude is given by [6]

$$U^{NR}_{Il_iJ_fJ_i}=A_{Il_iJ_fJ_i}F_{l_i}(k,a)G_{l_i}(k,a)J'_L, \tag{6}$$

$$A_{Il_iJ_fJ_i}=-(2)^{3/2}\,i^{l_i+L-l_f+1}\,e^{i(\omega_{l_i}-\phi_{l_i})}\frac{1}{k}\,\mu_{Bb}{}^{L+1/2}$$
$$\times\left(\frac{Z_b\,e}{m_b^L}+(-1)^L\frac{Z_B\,e}{m_B^L}\right)\sqrt{\frac{(L+1)(2L+1)}{L}}$$
$$\times\frac{1}{(2L+1)!!}(k_\gamma a)^{L+1/2}C_{J_fIl_f}W_{l_f}(2\kappa a)$$
$$\times\sqrt{P_{l_i}(E)}(l_i0\,L0|l_f0)U(Ll_fJ_iI;l_iJ_f), \tag{7}$$

$$J'_L(l_i\,l_f)=\frac{1}{a^2}\int_a^\infty dr\,r\,\frac{W_{l_f}(2\kappa r)}{W_{l_f}(2\kappa a)}$$
$$\times\left[\frac{F_{l_i}(k,r)}{F_{l_i}(k,a)}-\frac{G_{l_i}(k,r)}{G_{l_i}(k,a)}\right], \tag{8}$$

where a is the channel radius. $C_{J_fIl_f}$ is the asymptotic normalization coefficient, which defines the amplitude of the tail of the bound state wave function of nucleus A projected onto the two-body channel $B+b$ with the quantum numbers J_f, I, l_f. $W_l(2\kappa r)$ is the Whittaker hypergeometric function, $\kappa=\sqrt{2\mu_{Bb}\,\varepsilon_f}$ and l_f are the wave number and relative orbital angular momentum of the bound state, and $k_\gamma=E+\varepsilon_f$ is the momentum of the emitted photon. We use the system of units such that $\hbar=c=1$.

In a strict R-matrix approach, the resonant radiative width amplitude is divided into internal and channel parts,

$$[\Gamma^{J_i}_{\gamma J_f}(E)]^{1/2}=[\Gamma^{J_i}_{\gamma J_f}(E)]^{1/2}_{int}+[\Gamma^{J_i}_{\gamma J_f}(E)]^{1/2}_{ch}, \tag{9}$$

according to the channel radius. While the internal radiative width amplitude is real, the channel part is complex [6] and is defined as

$$[\Gamma^{J_i}_{\gamma J_f}(E)]^{1/2}_{ch}=\frac{-1}{\sqrt{2}}([F_{l_i}(k,a)]^2+[G_{l_i}(k,a)]^2)$$
$$\times\sqrt{\Gamma^{J_i}_{bIl_i}(E_R)}A_{Il_iJ_fJ_i}$$
$$\times\left(J''_L+I\frac{F_{l_i}(k,a)G_{l_i}(k,a)}{F^2_{l_i}(k,a)+G^2_{l_i}(k,a)}J'_L\right), \tag{10}$$

$$J''_L(l_i\,l_f)=\frac{1}{a^2}\int_a^\infty dr\,r\,\frac{W_{l_f}(2\kappa r)}{W_{l_f}(2\kappa a)}$$
$$\times\frac{F_{l_i}(k,r)F_{l_i}(k,a)+G_{l_i}(k,r)\,G_{l_i}(k,a)}{F^2_{l_i}(k,a)+G^2_{l_i}(k,a)}. \tag{11}$$

Both the nonresonant amplitude and the channel radiative width amplitude are normalized in terms of the ANC, $C_{J_fIl_f}$. Such a normalization is physically transparent: both quantities describe peripheral processes and, hence, contain the tail of the nuclear overlap function, whose normalization is given by the corresponding ANC. Note that the internal contribution to the nonresonant amplitude is included in the resonance term in the R-matrix method. Also, in the conventional R-matrix approach, the channel radiative width and nonresonant amplitude are normalized in terms of the reduced width amplitude, which is not directly observable and depends on the channel radius. However, it is more convenient to express the normalizations in terms of the ANC that can be measured independently [7]. Then only the radial matrix element depends on the channel radius.

Thus by measuring the ANC for the ground state of ^{12}N, we are able to fix the absolute normalization of the channel radiative width and nonresonant amplitudes simultaneously. The internal radiative width is determined by the nuclear many-body system. This contribution can be estimated from the experimental total radiative width and the channel radiative width based on Eq. (9).

III. EXPERIMENTAL PROCEDURE

The ^{11}C radioactive beam was produced via the reaction ^{1}H(^{11}B,^{11}C)n, using ~800 enA of 13 MeV/nucleon ^{11}B beam from the K500 superconducting cyclotron at Texas A&M University bombarding a 10-cm-long, LN_2-cooled, cryogenic H_2 gas cell with 12.7 μm Havar windows. ^{11}C recoils at 10 MeV/nucleon were collected by the Momentum Achromat Recoil Spectrometer (MARS) at 0°. They were separated from the primary beam and other reaction products and focused on the secondary target. For beam studies a 5×5 cm^2, 1000-μm-thick, position-sensitive silicon detector was mounted on the secondary target ladder. The detector consisted of 16 3-mm-wide resistive strips on one side that provided for both vertical and horizontal position measurements. The vertical position resolution along the resistive strips was better than 1 mm [full width at half maximum (FWHM)]. The total energy deposited in the detector was provided by a read out on the back plane. After tuning MARS, the secondary beam spot size and divergence were measured to be 3 mm (FWHM) and 1.8° (FW) in x and 3.2 mm (FWHM) and 1.9° (FW) in y. The energy spread of the beam was 1.6 MeV. The purity was better than 99%, with the primary contaminant being ^{7}Be. Secondary beam rates on target were typically over 400 kHz. For a detailed description of radioactive beam production with MARS, see Ref. [8].

The secondary reaction target consisted of 1.50 mg/cm^2 melamine ($C_3N_6H_6$) on 20-μg/cm^2 C and 20-μg/cm^2 collodion backings. The thickness and uniformity were verified by direct measurements with the ^{11}C beam by observing the beam energy spectrum with and without the target. With a peak shift of 2.46 MeV, the dE/dx calculation from the ion beam-target interaction program SRIM [9] gave the central target thickness to be 1.48 mg/cm^2 with an uncertainty of 6%, arising from the SRIM calculation and the statistical uncertainty from the peak shift.

The reaction products from ^{11}C bombarding the melamine target were recorded by two detector telescopes, each of which consisted of a 5×5-cm^2 16-strip position-

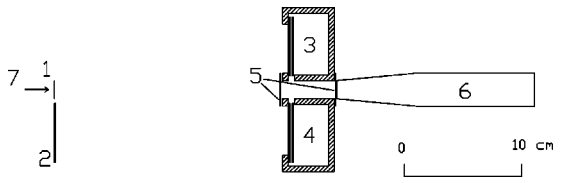

FIG. 2. Detector setup. (1) Melamine target. (2) Target detector. (3) Si detector telescope 1. (4) Si detector telescope 2. (5) 9% transparent screens. (6) Plastic scintillator detector with lucite light guide. (7) Incident ^{11}C beam.

sensitive Si detector with a thickness of 60 μm backed by a 500-μm Si detector. The telescopes were separated from the target by a distance of 200 mm. Both telescopes were cooled to -6°C to reduce thermal noise. To avoid beam hitting the detectors directly and to obtain a reasonable event rate for the transfer reaction, the two telescopes were separated by 28 mm. This distance was chosen by a Monte Carlo simulation based on the measured beam properties and a calculation of the elastic scattering reaction rate with the optical model code PTOLEMY [10]. A NE102A plastic scintillator coupled to a photomultiplier tube by a lucite light guide was mounted between these two Si telescopes to monitor the ^{11}C beam. Since the full beam intensity was too high for the scintillator, two screens, each with a transparency of 9%, were added to attenuate the beam intensity. The total effective attenuation, $\sim$ 98.5%, was measured in special runs that compared the ^{11}C yield observed in the target detector and the plastic scintillator detector for equal ^{11}B incident beam intensities. The details of the detector setup are shown in Fig. 2. With this geometry, the ^{11}C elastic scattering rate was about 10 Hz, and the ^{14}N(^{11}C, ^{12}N)$^{13}C_{g.s.}$ proton transfer reaction rate was above 100 per day.

IV. DATA ANALYSIS

After the calibration of the energy and position for the two telescopes, the particle identification (PID) vs. Q value was calculated for each event, as shown in Fig. 3. The PID was based on the measured energy loss in the ΔE detector and the total energy. The reconstructed Q value for reaction $A(a,b)B$ was calculated from

$$Q=\left(\frac{M_a}{M_B}-1\right)E_a+\left(\frac{M_b}{M_B}+1\right)E_b-2\frac{\sqrt{M_aM_bE_aE_b}}{M_B}\cos\theta. \tag{12}$$

Of course, the masses of the particles varied from reaction to reaction. For convenience, the Q value shown here was calculated assuming that all of the recoils corresponded to ^{11}C elastic scattering on ^{14}N. Consequently, the Q value is well focused for the elastic events, while it is slightly smeared for other channels. During our analysis, the Q values were calculated separately according to the channels of interest. Due to a thickness variation of the ΔE detectors, the PID varied at different locations by as much as 10%. This was large enough to degrade our isotope resolution. To eliminate this effect, each telescope was divided into a 16×16 grid. The PID of every event was normalized to the average ^{11}C PID according to the grid. Then the elastic and primary transfer channels were clearly separated from the other reaction products. The results shown in Fig. 3 were obtained after applying the thickness correction.

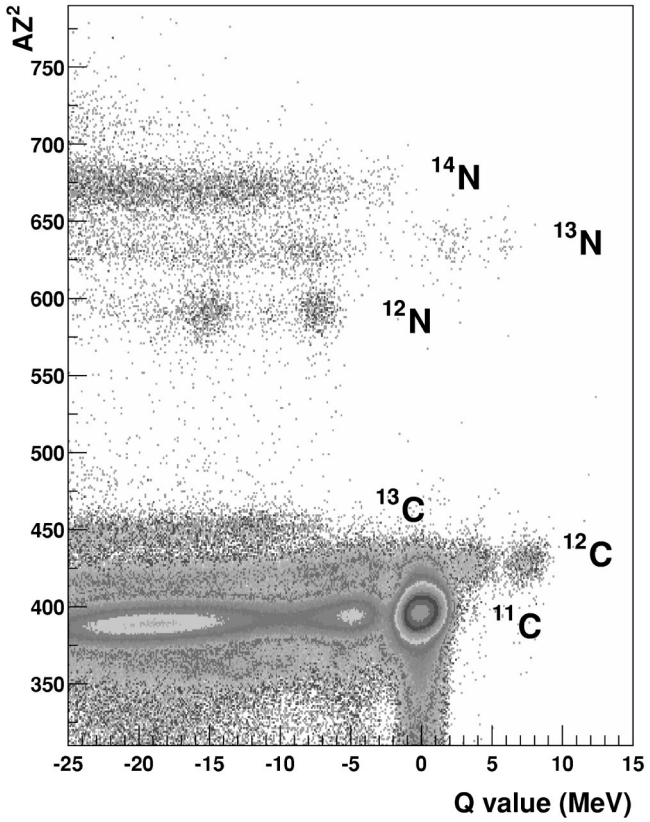

FIG. 3. The particle identification AZ^2 vs the Q value distribution, after applying the detector thickness correction described in the text. The ^{11}C group with Q value of 0 MeV is the elastic channel, and the least negative Q-value peak in ^{12}N is from ^{14}N(^{11}C, ^{12}N)$^{13}C_{g.s.}$.

The ^{11}C elastic scattering channel can be easily identified with its large yield at zero Q value. But it is not purely ^{11}C elastic scattering on ^{14}N nuclei since the melamine target also contained carbon and hydrogen. The maximum allowed scattering angle for ^{1}H(^{11}C, ^{11}C)^{1}H is 5.22°, while the detector system only covered angles between 4° and 17°. The kinematic shift of the ^{11}C recoils is large near the maximum angle, so this scattering process was easily separated from ^{14}N(^{11}C, ^{11}C)^{14}N using the energy difference. The other two elastic reactions, ^{14}N(^{11}C, ^{11}C)^{14}N and ^{12}C(^{11}C, ^{11}C)^{12}C, were indistinguishable at small angles due to the energy spread of the ^{11}C beam. During the analysis, a manual cut was set on the energy versus angle spectrum to accept both elastic processes, independent of scattering angle.

The first excited states of ^{11}C, ^{14}N and ^{12}C are at 2.0, 2.31, and 4.44 MeV, respectively. The transition between the ground state of ^{14}N and the first excited state is a pure $M1$ transition. Inelastic excitation of this state was found to be weak in a previous study of ^{13}C(^{14}N, ^{14}N)^{13}C at a similar energy [11], and it is expected to be weak in the present case also. The transition between the ^{12}C ground state and the

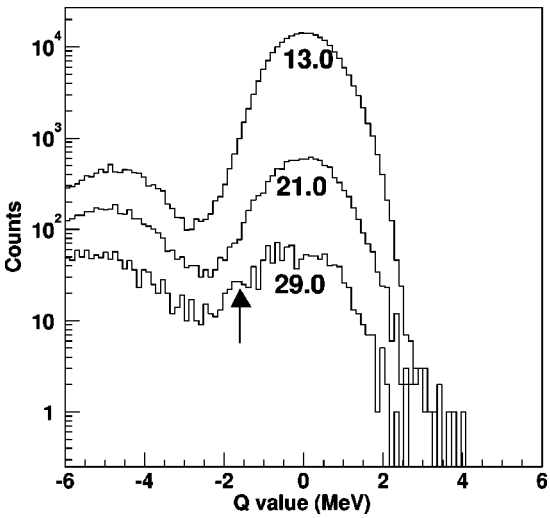

FIG. 4. Selected Q value spectra for ^{11}C around the elastic channel in 2 ° angle bins in the center-of-mass frame. The central angles are shown beneath each curve. The inelastic scattering, ^{12}C (^{11}C, ^{11}C)^{12}C*, is clearly observed with a Q value near -5 MeV in each angle bin. For the 29° angle bin, the energy difference between ^{14}N(^{11}C, ^{11}C)^{14}N and ^{12}C (^{11}C, ^{11}C)^{12}C can be observed, and the small peak noted with an arrow may arise from ^{11}C inelastic scattering off ^{14}N or ^{12}C.

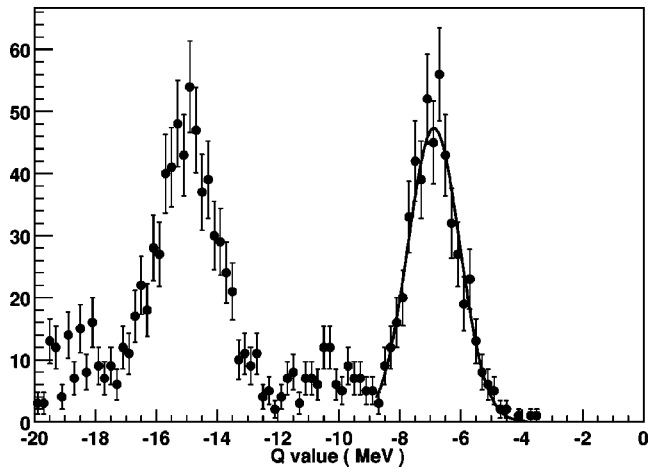

FIG. 5. Q value spectrum for ^{12}N reaction products. The peak at -6.9 MeV is from ^{14}N(^{11}C, ^{12}N)$^{13}C_{g.s.}$. The peak near -10.5 MeV reflects population of ^{13}C excited states. The peak at -15.0 MeV is from ^{12}C(^{11}C, ^{12}N)$^{11}B_{g.s.}$

first excited state is a collective $E2$ transition. It was a strong inelastic process in our experiment and appears as a ^{11}C peak with a Q value around -5 MeV in Figs. 3 and 4. The shift of the Q value is due to the assumption that scattering occurred off of ^{14}N. The transition between the ^{11}C ground state and the first excited state is an $M1+E2$ transition. According to an estimate by Descouvemont [12], the $E2$ transition can be as large as 9.8 Weisskopf units, which implies that inelastic excitation of this state could make a significant contribution to the spectrum near the elastic scattering peak. To investigate the effects of inelastic reactions near the elastic peak, the Q value spectrum for ^{11}C was generated in 2 ° angle bins in the center of mass. The results are shown for selected bins in Fig. 4. Inelastic scattering to the 4.44 MeV state in ^{12}C is clearly observed. At large angles, the energy difference between the elastic scattering of ^{11}C on ^{12}C and ^{14}N can be observed, and a small additional peak may arise from the inelastic excitation of ^{11}C off of ^{14}N or ^{12}C. In our analysis, all ^{11}C events with a Q value greater than -2 MeV were considered to be due to elastic scattering off of ^{14}N or ^{12}C. This criterion may overestimate the elastic events, particularly at larger scattering angles, due to a possible contribution from the excitation of ^{11}C.

No bound excited states of ^{12}N exist, so only proton transfer reactions leading to the ground state could be observed. The energy of the first excited state of ^{13}C is 3.0 MeV. Thus transfer reactions leading to excited states of ^{13}C should be clearly separated from ^{14}N (^{11}C, ^{12}N)$^{13}C_{g.s.}$. The Q value spectrum for ^{12}N from the reactions between ^{11}C and the melamine target is shown in Fig. 5. The Q value peak from ^{14}N (^{11}C, ^{12}N)$^{13}C_{g.s.}$ is well separated from the other reaction products. The small yield around -10.5 MeV is due to reactions leading to excited states of ^{13}C. The peak at a Q value of -15.0 MeV is from the ^{12}C(^{11}C, ^{12}N)$^{11}B_{g.s.}$ reaction. In the discussion below, only elastic scattering and the ^{14}N(^{11}C, ^{12}N)$^{13}C_{g.s.}$ proton transfer reaction are considered.

V. ELASTIC SCATTERING AND OPTICAL-MODEL POTENTIALS

The experimental elastic scattering cross section is shown in Fig. 6 together with optical-model calculations done with two different sets of parameters. Both calculations have been smoothed to account for finite angular acceptance. Since we cannot distinguish between the elastic scattering of ^{11}C off of ^{14}N or ^{12}C in the melamine target, the two reaction channels were summed together in the laboratory scattering frame according to their atomic ratios, then the combined result was converted to the center-of-mass frame using the kinematics appropriate for ^{11}C+ ^{14}N. The optical-model parameters were obtained from double-folding-model calculations [13]. The folded potentials were renormalized to match the systematics observed in elastic scattering of *p*-shell nuclei at 9 to 16 MeV/nucleon. For loosely-bound nuclei (at least one nucleus has very low minimum separation energy below $\sim$ 2.5 MeV), the renormalization parameters were found to be $N_V=0.366$ and $N_W=1.000$. For tightly-bound nuclei (minimum separation energies well above 2.5 MeV), the renormalization parameters are $N_V=0.455$ and $N_W=0.844$. In this paper, both sets were used to compare with the experimental data. The forward elastic scattering cross section, which is dominated by Coulomb scattering, is not very sensitive to the optical-model parameters. The difference between the two predictions for angles less than 12° is $\sim$ 4.2%. Furthermore, varying the normalization factors for the ^{11}C+^{12}C and ^{11}C+^{14}N real and imaginary potentials within their uncertainties as in Ref. [13] only resulted in a 2.6% change in the elastic cross section for these angles. Therefore, this region is used to examine the absolute normalization. The overall differences between the best fit to the first three experimental

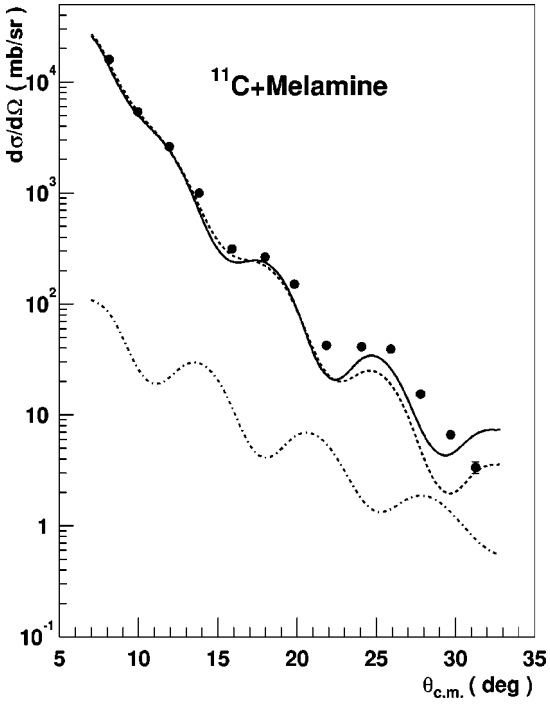

FIG. 6. Elastic scattering angular distributions for ^{11}C on melamine. The experimental result is shown as dots with statistical uncertainty only. There is an additional 6.5% normalization uncertainty that is common for all the data points. Two sets of predicted distributions are shown. The solid curve used the parameters for tightly-bound nuclei, while the dashed curve used those for loosely-bound nuclei. The dash-dotted curve is the prediction for ^{14}N(^{11}C, ^{11}C*)^{14}N with a $B(E2)$ of ten Weisskopf units.

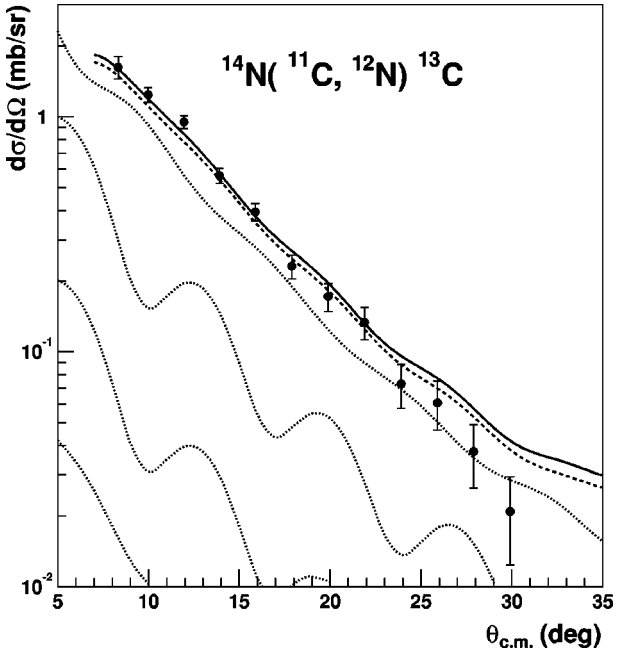

FIG. 7. Transfer reaction angular distributions for ^{14}N(^{11}C, ^{12}N)^{13}C$_{g.s.}$. Two sets of predicted DWBA angular distributions are shown. The solid curve used the parameters for tightly-bound nuclei for the incoming channel and those for loosely bound nuclei for the outgoing channel. The dashed curve used the parameters for loosely-bound nuclei for both the incoming and outgoing channels and the same ANC as found from the fit using the solid curve. The four dotted curves show the separate contributions from Eq. (13), before correcting for finite angular resolution. From top to bottom, they represent the ^{14}N($p_{1/2}$)$\rightarrow$ ^{12}N($p_{1/2}$), ^{14}N($p_{1/2}$) $\rightarrow$ ^{12}N($p_{3/2}$), ^{14}N($p_{3/2}$)$\rightarrow$ ^{12}N($p_{1/2}$), and ^{14}N($p_{3/2}$)$\rightarrow$ ^{12}N($p_{3/2}$) proton transfer reactions.

data points and the predictions in Fig. 6 are within 5%, which is consistent with the previous estimate for the uncertainty arising from the incident beam normalization and target thickness.

The optical-model prediction for tightly-bound nuclei provides a better description of the elastic scattering at angles beyond 20° than that for loosely-bound nuclei. This is reasonable since ^{11}C is tightly bound when compared with nuclei such as ^{8}B and ^{12}N. Both the first excited state and proton separation energies in ^{11}C are large compared to the loosely-bound *p*-shell nuclei used in the elastic scattering studies of Ref. [13]. In the following DWBA calculations, the parameters for tightly-bound nuclei were adopted for the incident channel, ^{11}C+^{14}N.

To investigate the influence from inelastic scattering of ^{11}C, the reaction ^{14}N(^{11}C, ^{11}C*)^{14}N was calculated with PTOLEMY [10] using a $B(E2)$ of ten Weisskopf units. The result is shown in Fig. 6. Clearly the contribution from this process is negligible for small angles, but it may contribute at angles larger than 25°. As shown in Fig. 4, inelastic ^{11}C events just below the elastic scattering peak may be observed in the *Q* value spectrum for $28° < \theta_{c.m.} < 30°$, where the predicted ratio of inelastic to elastic scattering cross sections becomes a maximum. Only the last few angle bins showed any hint of inelastic excitation of ^{11}C. We did not attempt to remove these events from the elastic yield via peak fitting since we could not do this in a systematic way. Consequently, the experimental ^{11}C elastic scattering cross section on the melamine target may be slightly overestimated at large angles. However, this is not likely to account for the full difference between the experimental result and the optical model prediction at large scattering angles.

VI. ^{14}N(^{11}C, ^{12}N)^{13}C ANGULAR DISTRIBUTION AND ANC FOR ^{12}N $\leftrightarrow$ ^{11}C+*p*

The angular distribution for the ^{14}N(^{11}C, ^{12}N)^{13}C reaction is shown in Fig. 7. The solid curve is a DWBA prediction for the proton transfer reaction that uses the tightly-bound optical-model parameters for ^{11}C+^{14}N and the loosely-bound parameters for ^{12}N+^{13}C. In the DWBA calculation, the ratio of the two ANC components $(C^{^{12}N}_{p_{3/2}})^2/(C^{^{12}N}_{p_{1/2}})^2$ [$\mathcal{F}$ in Eq. (13)] was put at 0.17/0.71, which was obtained from shell model calculations [14]. The ANCs for ^{14}N$\leftrightarrow$^{13}C+*p* were determined to be $C^2_{p_{1/2}} = 18.2 \pm 0.9$ fm^{-1} and $C^2_{p_{3/2}} = 0.91 \pm 0.14$ fm^{-1} in previous studies of ^{13}C(^{14}N, ^{13}C)^{14}N [11] and ^{13}C(^{3}He, *d*)^{14}N [15].

By normalizing the predictions to the experimental data [16],

$$\sigma_{exp}=(C^{^{12}N}_{p_{1/2}})^2\left[\left(\frac{C^{^{14}N}_{p_{1/2}}}{b^{^{12}N}_{p_{1/2}}b^{^{14}N}_{p_{1/2}}}\right)^2\sigma^{DW}_{p_{1/2},p_{1/2}}+\left(\frac{C^{^{14}N}_{p_{3/2}}}{b^{^{12}N}_{p_{1/2}}b^{^{14}N}_{p_{3/2}}}\right)^2\sigma^{DW}_{p_{1/2},p_{3/2}}+\mathcal{F}\left(\frac{C^{^{14}N}_{p_{1/2}}}{b^{^{12}N}_{p_{3/2}}b^{^{14}N}_{p_{1/2}}}\right)^2\sigma^{DW}_{p_{3/2},p_{1/2}}+\mathcal{F}\left(\frac{C^{^{14}N}_{p_{3/2}}}{b^{^{12}N}_{p_{3/2}}b^{^{14}N}_{p_{3/2}}}\right)^2\sigma^{DW}_{p_{3/2},p_{3/2}}\right], \quad (13)$$

the values of the ANC's for $^{12}\mathrm{N}\leftrightarrow{}^{11}\mathrm{C}+p$ were found to be $C^2_{p_{1/2}}=1.4\pm0.2$ fm^{-1} and $C^2_{p_{3/2}}=0.33\pm0.05$ fm^{-1}. The uncertainties for σ_{exp} in Eq. (13) include statistics (3.0%) and absolute normalization of the cross section (6.5%). The uncertainties contributed by the inputs to the Monte Carlo simulation were investigated by varying the beam center within its uncertainty and rotating the angle of the detectors within 1°. The overall uncertainty from these effects is 2.0%. By changing the normalization constants of the real and imaginary optical potentials for the incoming and outgoing channels within their uncertainties from Ref. [13], the variation of the DWBA calculations was found to be less than 8.0%. A comparison of the DWBA calculations to others that adopted the optical-model parameters for loosely-bound nuclei in the entrance channel (see Fig. 7) contributed an additional 4%. The knowledge of the $^{14}\mathrm{N}\leftrightarrow{}^{13}\mathrm{C}+p$ ANC's introduced an uncertainty of 6.4%. Combining these gives a total uncertainty of 13%. The individual ANC's also depend on the theoretical prediction of $\mathcal{F}$. A variation of $\mathcal{F}$ within $\pm20\%$ leads to a $\mp5.2\%$ change in the inferred value of $(C^{^{12}N}_{p_{1/2}})^2$ and a $\pm14.8\%$ change in the inferred value of $(C^{^{12}N}_{p_{3/2}})^2$. Given this anti-correlation, the overall $^{11}\mathrm{C}(p,\gamma)^{12}\mathrm{N}$ direct capture rate, which depends on the linear combination $C^2_{p_{eff}}=C^2_{p_{1/2}}+C^2_{p_{3/2}}=1.73\pm0.25$ fm^{-1} is essentially independent of the choice for $\mathcal{F}$.

VII. ANC AND RADIATIVE WIDTH

The ANC gives useful information not only about the overall normalization of the direct capture amplitude, but also about the radiative width of the resonances. According to Eqs. (7) and (10), the channel part of the radiative width may be determined from the ANC. Since the channel part is complex, i.e. $[\Gamma^{J_i}_{\gamma J_f}(E)]^{1/2}_{ch}=a+ib$, while the internal part is real, i.e., $[\Gamma^{J_i}_{\gamma J_f}(E)]^{1/2}_{int}=c$, the total radiative width can be written as

$$\Gamma^{J_i}_{\gamma J_f}(E)=(a+c)^2+b^2. \quad (14)$$

The relative phase of a and c is, *a priori*, unknown, so these real parts may interfere either constructively or destructively. Hence, b^2 always provides a lower limit for the radiative width, and additional stronger limits may be obtained if assumptions are made about the interference between the two real contributions. For constructive interference of the real parts, the channel contribution gives a stronger lower limit. In the case of destructive interference, if $|a|>|c|$, the channel contribution gives an upper limit for the radiative width. These limits depend on only one model parameter, the channel radius.

The radiative width of the second resonance in ^{12}N decaying to the ground state has been a controversial subject theoretically [2,12]. The experiment at GANIL [4] found $\Gamma_\gamma=6.0^{+7}_{-3.5}$ meV. Recently, a measurement at RIKEN [5] found 13.0 ± 0.5 meV. It is informative to see how the measured ANC for ^{12}N imposes limits on the radiative width of the second resonance with respect to the experimental value. We find that $\Gamma^{J_i}_{\gamma J_f}(E_R)_{ch}=54$ meV for a channel radius of $a=5.0$ fm. Taking into account the experimental value of the total radiative width, one can find the internal contribution from Eq. (14). There are two solutions, 15 and 112 meV. Assuming that the second value is too high [17], we conclude that the internal part of the radiative width is 15 meV, and destructive interference between the real parts of the channel and internal contributions gives the experimental value, 13 meV. In this case, the channel contribution alone represents an upper limit for the radiative width, while the square of the imaginary part of the channel contribution, 1.8 meV, gives a lower limit.

The relative phase between the direct capture amplitude and the channel contribution to the γ width of the second resonance is fixed in the R-matrix approach [see Eqs. (6) and (10)]. Therefore, when the channel contribution to the γ width dominates, the sign of the interference effects may be determined unambiguously. For $^{11}\mathrm{C}\ (p,\gamma)\,^{12}\mathrm{N}$, we find that the nonresonant and resonant capture amplitudes interfere constructively below the resonance and destructively above it.

VIII. S FACTOR FOR $^{11}\mathrm{C}\ (p,\gamma)\,^{12}\mathrm{N}$

The summed cross section for nonresonant capture and resonant capture through the broad second excited state was calculated from the measured ANC and the experimental resonance parameters using the R-matrix approach. The cross section due to capture through the first resonance was estimated separately with the Breit-Wigner formula. In the calculations, the experimental proton widths were taken from Ref. [18]. Only an upper limit of 20 keV is available for the proton width of the first excited state. It was set to 5.5 keV, as suggested in Ref. [4], but the contribution from this narrow resonance over the region of interest only depends on Γ_γ. The Γ_γ width for this resonance was set at 2.6 meV, as adopted in Refs. [2,4]. Its uncertainty was assumed to be the same as that of the lifetime of the first excited state of ^{12}B.

The updated S factor is shown together with the GANIL result in Fig. 8. The upper solid line gives our result for the total S factor. The relatively flat lower solid line, which is our result for direct capture alone, is slightly larger than the GANIL result at energies less than 0.25 MeV, but it is much

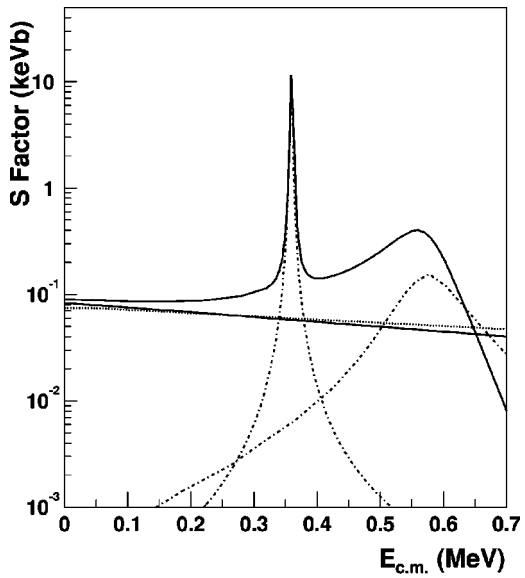

FIG. 8. *S* factor for $^{11}\mathrm{C}(p,\gamma)^{12}\mathrm{N}$. The upper solid line is our updated *S* factor. Our direct capture contribution is shown as the lower solid line. For comparison, the direct capture result from the GANIL measurement [4] is shown as the dotted line, and the resonant contributions, which were treated as noninterfering in Ref. [4], are shown by dash-dotted lines.

more precise. We find no change in the contribution from the first resonance compared to the GANIL analysis, but the contribution from the second resonance is larger by a factor of about 2.5. The low energy *S* factor is enhanced by the interference between direct capture and resonant capture to the second excited state.

The uncertainties in the astrophysical *S* factor were investigated by varying the ANC for $^{12}\mathrm{N}$, Γ_γ of the first resonance, the total width Γ_{total} of the second resonance, and Γ_γ of the second resonance within their respective uncertainties. Also the channel radius was varied from 4.5 fm to 5.5 fm. Only the ANC, Γ_γ of the first resonance, and the total width of the second resonance are found to make significant contributions to the uncertainty for $E_{c.m.}<0.7$ MeV. The effects of these uncertainties on the astrophysical *S* factor are shown in Fig. 9. At energies below 400 keV, the total uncertainty is less than 20%.

IX. REACTION RATE OF $^{11}\mathrm{C}(p,\gamma)^{12}\mathrm{N}$

The astrophysical reaction rate [19] for the sum of nonresonant capture and the second wide resonance was calculated with

$$N_A\langle\sigma v\rangle_{NR}=N_A\left(\frac{8}{\pi\mu}\right)^{1/2}\left(\frac{1}{kT}\right)^{3/2}\times\int_0^\infty S(E)e^{([-\sqrt{E_G/E}-(E/kT)])}dE, \quad (15)$$

and the reaction rate for the first narrow resonance was calculated with

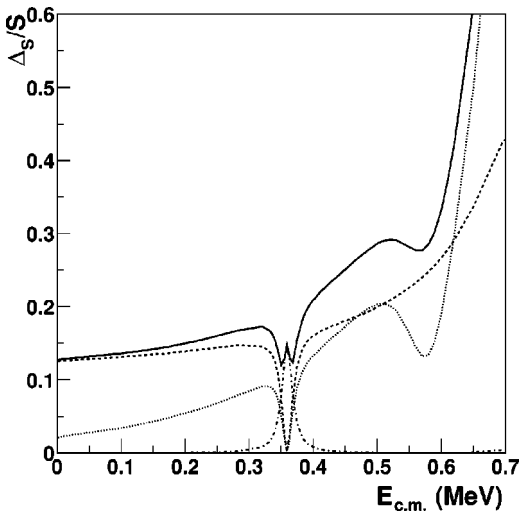

FIG. 9. Important contributions to the fractional uncertainty in the *S* factor. The contributions from the ANC (dashed line), the Γ_{total} of the second resonance (dotted line), and the γ transition width of the first resonance (dashed-dotted line) are shown, together with the total uncertainty (solid line).

$$N_A\langle\sigma v\rangle_R=N_A\left(\frac{2\pi}{\mu kT}\right)^{3/2}\hbar^2\times\frac{(2J+1)}{(2J_p+1)(2J_{^{11}\mathrm{C}}+1)}\frac{\Gamma_\gamma\Gamma_p}{\Gamma}e^{(-E_R/kT)}. \quad (16)$$

In Eqs. (15) and (16), N_A is Avogadro's number, and E_G is the Gamow energy [19]. In Eq. (16), $\Gamma_p\approx\Gamma$, so the reaction rate for this narrow resonance depends only on its γ transition width. The rate of the first resonance was fit with

$$N_A\langle\sigma v\rangle_R=\frac{1.670\times10^2}{T_9^{3/2}}e^{(-4.166/T_9)}\ \mathrm{cm^3\ s^{-1}\ mol^{-1}}, \quad (17)$$

while the summed rate for nonresonant capture and the second resonance was fit with

$$N_A\langle\sigma v\rangle_{NR}=\frac{2.148\times10^5}{T_9^{2/3}}\exp\left(-\frac{13.281}{T_9^{1/3}}\right)\times(1+4.639T_9^{1/3}-2.641T_9^{2/3}-1.543T_9+2.030T_9^{4/3}+4.657T_9^{5/3})\ \mathrm{cm^3\ s^{-1}\ mol^{-1}}. \quad (18)$$

The overall fitting errors were less than 3% in a range from $T_9=0.05$ to 0.6. The sum of the nonresonant contribution and capture from the second resonance completely dominates for the temperature region below $T_9=0.2$, and they contribute more than 55% to the rate over the range from $T_9=0.2$ to $T_9=0.4$.

Descouvemont argued in Ref. [12] that the radiative width of the first excited state in $^{12}\mathrm{N}$ was overestimated based on the result in $^{12}\mathrm{B}$, since charge symmetry is not an accurate approximation for $M1$ transitions. His microscopic model

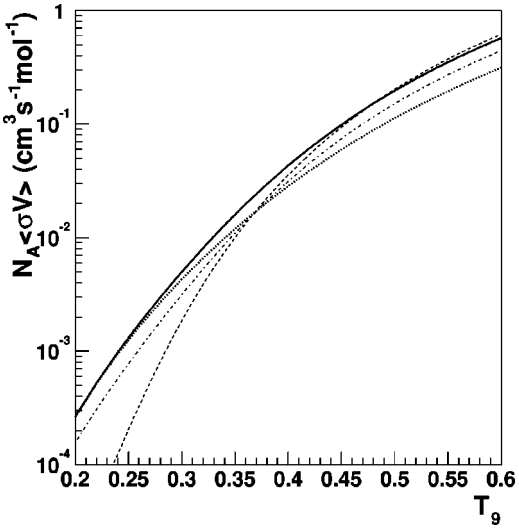

FIG. 10. Reaction rate for $^{11}C(p,\gamma)^{12}N$. The solid line shows our result when using $\Gamma_\gamma = 2.6$ meV for the first resonance. The dotted line shows our result when using $\Gamma_\gamma = 0.67$ meV. The dashed line is from Wiescher *et al.* [2], and the dash-dotted line is the GANIL result [4].

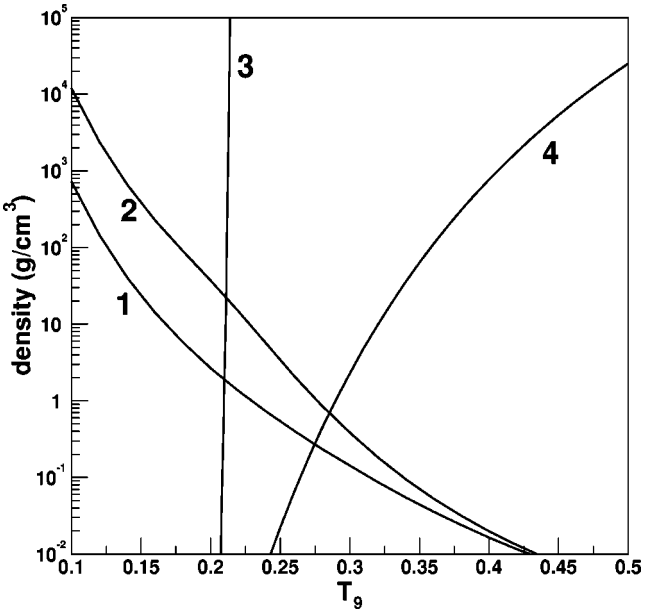

FIG. 11. The temperature and density conditions where the $^{11}C\ (p,\gamma)^{12}N$ reaction is important. Curve 1 shows where the rates for ^{11}C proton capture, based on the solid curve in Fig. 10, and beta decay will be equal. The proton capture reaction will dominate over beta decay above this curve. Curve 2 shows the previous estimate by Wiescher *et al.* [2]. In addition, the temperature must be to the right of curve 3 to permit the $^7Be(\alpha,\gamma)^{11}C$ reaction to produce ^{11}C effectively, and the density must be above curve 4 to produce ^{12}N faster than it can be photo-dissociated.

provided a lower value of 0.67 meV for the width in ^{12}N. This would reduce the contribution of the first resonance to the astrophysical reaction rate by a factor of 4. In this case, the first resonance can be neglected for the temperature region below $T_9 = 0.35$, and it contributes less than 30% to the rate at $T_9 = 0.6$.

The sum of the reaction rates is shown in Fig. 10, together with the previous results. The contributions to the uncertainty in the revised reaction rate were determined by using the uncertainties in the *S* factor as described above. The overall uncertainty is approximately 14% for $0.05 < T_9 < 0.6$. At $T_9 = 0.2$, our result is more than 1.7 times that obtained by the GANIL group and 14 times larger than the estimate of Wiescher *et al.*

X. CONCLUSION

Calculations based on consideration of traditional reaction sequences have set limits on the initial mass and metallicity that the stars can have without imploding with no significant mass loss. The $^3He(\alpha,\gamma)^7Be(\alpha,\gamma)^{11}C$ reactions are the main path other than the 3α process from helium to carbon isotopes in such stars. The ^{11}C produced in this sequence may decay and return to ^4He via $^{11}C\ (\beta^+\nu)^{11}B(p,\alpha)^8Be(^4He,^4He)$ or be depleted by proton capture into the $A \geqslant 12$ region through $^{11}C\ (p,\gamma)^{12}N$.

Our revised reaction rate for $^{11}C\ (p,\gamma)^{12}N$ implies that it will compete successfully with $^{11}C\ (\beta^+\nu)$ at lower densities than previously believed, as shown in Fig. 11. Therefore, the reaction sequence $^7Be\ (\alpha,\gamma)^{11}C\ (p,\gamma)\ ^{12}N$ will provide a means to produce CNO nuclei, while bypassing the 3α reaction, in lower-density environments than anticipated by Wiescher *et al.* Detailed understanding of the implications of the new reaction rates relies on new hydrodynamical calculations with the updated reaction sequences.

ACKNOWLEDGMENTS

This work was supported in part by the U.S. Department of Energy under Grant No. DE-FG03-93ER40773, the U.S. National Science Foundation under Grant No. INT-9909787 and project ME 385(2000), MSMT, CR, Grant No. GACR 202/01/0709, the Robert A. Welch Foundation, and NSF award No. PHY-0140343.

[1] G. M. Fuller, S. E. Woosley, and T. A. Weaver, Astrophys. J. **307**, 675 (1986).
[2] M. Wiescher, L. Buchmann, and F.-K. Thielemann, Astrophys. J. **343**, 352 (1989).
[3] C. L. Fryer, S. E. Woosley, and A. Heger, Astrophys. J. **550**, 372 (2001).
[4] A. Lefebvre *et al.*, Nucl. Phys. **A592**, 69 (1995).
[5] T. Minemura *et al.*, RIKEN Accel. Prog. Rep. **A35**, (2002).
[6] F. C. Barker and T. Kajino, Aust. J. Phys. **44**, 369 (1991).
[7] A. M. Mukhamedzhanov and R. E. Tribble, Phys. Rev. C **59**, 3418 (1999).
[8] A. Azhari, V. Burjan, F. Carstoiu, C. A. Gagliardi, V. Kroha, A. M. Mukhamedzhanov, F. M. Nunes, X. Tang, L. Trache, and R. E. Tribble, Phys. Rev. C **63**, 055803 (2001).

[9] James F. Ziegler, SRIM – the Stopping and Range of Ions in Matter, http://www.srim.org
[10] M. Rhoades-Brown, M. H. Macfarlane, and S. C. Pieper, Phys. Rev. C **21**, 2417 (1980); **21**, 2436 (1980).
[11] L. Trache, A. Azhari, H. L. Clark, C. A. Gagliardi, Y.-W. Lui, A. M. Mukhamedzhanov, R. E. Tribble, and F. Carstoiu, Phys. Rev. C **58**, 2715 (1998).
[12] P. Descouvemont, Nucl. Phys. **A584**, 532 (1995).
[13] L. Trache, A. Azhari, H. L. Clark, C. A. Gagliardi, Y.-W. Lui, A. M. Mukhamedzhanov, R. E. Tribble, and F. Carstoiu, Phys. Rev. C **61**, 024612 (2000).
[14] S. Cohen and D. Kurath, Nucl. Phys. **A101**, 1 (1967).
[15] P. Bém, V. Burjan, V. Kroha, J. Novák, Š. Piskoř, E. Šimečková, J. Vincour, C. A. Gagliardi, A. M. Mukhamedzhanov, and R. E. Tribble, Phys. Rev. C **62**, 024320 (2000)
[16] A. M. Mukhamedzhanov, H. L. Clark, C. A. Gagliardi, Y.-W. Lui, L. Trache, R. E. Tribble, H. M. Xu, X. G. Zhou, V. Burjan, J. Cejpek, V. Kroha, and F. Carstoiu, Phys. Rev. C **56**, 1302 (1997).
[17] P. Descouvemont, Nucl. Phys. **A646**, 261 (1999).
[18] F. Ajzenberg-Selove, Nucl. Phys. **A506**, 1 (1990).
[19] C. Rolf and W. Rodney, *Cauldrons in the Cosmos* (University of Chicago Press, Chicago, 1988).